


## RESEARCH ARTICLE

# Regulating the interfacial chemistry of graphite in ethyl acetate-based electrolyte for low-temperature Li-ion batteries

Ling Che<sup>1</sup> | Zhaowen Hu<sup>1</sup> | Tao Zhang<sup>1</sup> | Peiming Dai<sup>1</sup> | Chengyu Chen<sup>1</sup> |  
Chao Shen<sup>1</sup> | Haitao Huang<sup>2</sup> | Lifang Jiao<sup>3</sup> | Ting Jin<sup>1,2,3</sup>  | Keyu Xie<sup>1</sup>

<sup>1</sup>State Key Laboratory of Solidification Processing, School of Materials Science and Engineering, Center for Nano Energy Materials, Northwestern Polytechnical University and Shaanxi Joint Laboratory of Graphene (NPU), Xi'an, China

<sup>2</sup>Department of Applied Physics and Research Institute for Smart Energy, The Hong Kong Polytechnic University, Hong Kong, China

<sup>3</sup>Key Laboratory of Advanced Energy Materials Chemistry (Ministry of Education), Renewable Energy Conversion and Storage Center (ReCast) College of Chemistry, Nankai University, Tianjin, China

## Correspondence

Ting Jin and Keyu Xie, State Key Laboratory of Solidification Processing, School of Materials Science and Engineering, Center for Nano Energy Materials, Northwestern Polytechnical University and Shaanxi Joint Laboratory of Graphene (NPU), Xi'an 710072, China.  
Email: [tjin@nwpu.edu.cn](mailto:tjin@nwpu.edu.cn) and [kyxie@nwpu.edu.cn](mailto:kyxie@nwpu.edu.cn)

## Funding information

Fundamental Research Funds for the Central Universities,  
Grant/Award Number: 3102019JC005; National Key Research and Development Program of China, Grant/Award Number: 2023YFE0203000; Hong Kong Polytechnic University, Grant/Award Number: G-YZ4S; Natural Science Foundation of Chongqing, Grant/Award Number: CSTB2022NSCQ-MSX0596; Natural Science Basic Research Plan in Shaanxi Province of China, Grant/Award Number: 2022JQ-086; Hong Kong Scholars Program, Grant/Award Number: XJ2021040

## Abstract

Lithium-ion batteries suffer from severe capacity loss and even fail to work under subzero temperatures, which is mainly due to the sluggish Li<sup>+</sup> transportation in the solid electrolyte interphase (SEI) and desolvation process. Ethyl acetate (EA) is a highly promising solvent for low-temperature electrolytes, yet it has poor compatibility with graphite (Gr) anode. Here, we tuned the interfacial chemistry of EA-based electrolytes via synergies of anions. ODFB<sup>−</sup> with low solvation numbers, participates in the solvation sheath, significantly reducing the desolvation energy. Meanwhile, combined with the high dissociation of FSI<sup>−</sup>, the reduction of both anions constructs an inorganic-rich SEI to improve interfacial stability. The electrolyte enables Gr anode to deliver a capacity of 293 mA h g<sup>−1</sup> and 2.5 Ah LiFePO<sub>4</sub>||Gr pouch cell to exhibit 96.85% capacity retention at −20°C. Remarkably, LiFePO<sub>4</sub>||Gr pouch cell with the designed electrolyte can still retain 66.28% of its room-temperature capacity even at −40°C.

## KEYWORDS

ethyl acetate (EA), graphite, inorganic-rich SEI, lithium-ion batteries, low-temperature electrolyte

## 1 | INTRODUCTION

Graphite (Gr)-based lithium-ion batteries (LIBs) have been widely applied in 3C portable devices and electric vehicles (EVs) owing to their high energy/power density, long lifespan, and environmental friendliness.<sup>1,2</sup> However, they encounter severe capacity loss, difficulty charging and even fail to work under subzero temperatures.<sup>3</sup> For example, the typical 18650 Li-ion cell can only retain ~5% of energy density at  $-40^{\circ}\text{C}$ .<sup>4</sup> In addition, due to the polarization of Gr-based LIBs under low temperatures,  $\text{Li}^+$  ions are difficult to intercalate into the Gr electrode but deposit on the surface of the Gr electrode to form lithium dendrites, bringing safety issues to battery system.<sup>5–7</sup> Accordingly, the low-temperature performance of Gr-based LIBs is urgently needed to be improved for their application in EVs, subsea operations, military and defense, as well as space exploration areas.<sup>8–10</sup>

Previous studies have demonstrated that the issues of LIBs under low temperatures are reflected in the following aspects: (1) The increased viscosity and decreased ionic conductivity of electrolytes; (2) the drastically increased solid electrolyte interphase (SEI) resistance ( $R_{\text{SEI}}$ ) and charge transfer resistance ( $R_{\text{ct}}$ ); (3) the sluggish  $\text{Li}^+$  diffusion in the bulk electrode materials.<sup>11,12</sup> Among them, the behaviors of  $\text{Li}^+$  ions on the anode/electrolyte interphase are regarded as the most sluggish process during the charge process in LIBs.<sup>13</sup> The electrolyte, as an indispensable component in LIBs, not only affects  $\text{Li}^+$  transport but also largely determines the properties of electrode/electrolyte interphase, which is responsible for the low-temperature performance of LIBs to a large extent.<sup>14,15</sup> Therefore, it is urgently appealed to develop advanced electrolytes with high ionic conductivity and low interfacial impedance at low temperatures. Up to now, ethylene carbonate (EC), in terms of its good film-forming properties and dissolving ability of lithium salts, is still deemed to be a usual ingredient in the electrolyte of commercial Gr-based LIBs.<sup>16,17</sup> But unfortunately, EC has a high melting point ( $36^{\circ}\text{C}$ ) and a strong affinity with  $\text{Li}^+$ , which severely affects  $\text{Li}^+$  diffusion in electrolytes and the desolvation of  $\text{Li}^+$  on Gr/electrolyte interphase, thus leading to the deterioration of low-temperature performance in LIBs.<sup>18</sup> In this regard, various solvents with low melting point and low viscosity (such as linear carboxylates, linear carbonates, ethers, etc.) have been widely exploited in the electrolytes to improve the low-temperature properties of LIBs.<sup>19,20</sup> Among them, ethyl acetate (EA) is a favorable candidate owing to its ultra-low freezing point ( $-84^{\circ}\text{C}$ ) and suitable dielectric constant (6.4).<sup>21</sup> Unfortunately, the decomposition of EA forms a thick SEI with high resistance on the Gr anodes. For the regulation strategy of interface chemistry for EA-based

electrolytes, high-concentration electrolytes (HCEs), localized HCEs, or fluorinated electrolytes are common.<sup>12,22–25</sup>

Li et al. developed a 3 M EA-based electrolyte, which achieved a record-breaking cycle life of more than 1 year.<sup>23</sup> Yoo et al.<sup>24</sup> altered the fluorination position and degree of EA, resulting in low binding energy with  $\text{Li}^+$ . However, the above-mentioned strategies not only increase the viscosity of the electrolytes, which is adverse to low-temperature performances, but also greatly increase the cost of the electrolytes, limiting their practical application.

Herein, we designed a dual-anion regulated weakly solvated EA-based electrolyte, which employs lithium bis (fluorosulfonyl)imide (LiFSI) and lithium difluoro(oxalato)borate (LiODFB) to cooperatively improve the low-temperature performance of LIBs. Based on the conventional-concentration (1 M) electrolyte, ODFB<sup>−</sup> participates in  $\text{Li}^+$  solvation sheath to form contact ion pairs (CIP) structure, resulting in low desolvation energy. Additionally, FSI<sup>−</sup>, with high dissociation, can increase the ionic conductivity at low temperatures. Furthermore, the dual-anion regulated electrolyte promotes the formation of inorganic-rich SEI, which improves the compatibility of EA-based electrolytes with Gr anode. As a result, the Gr anode in the electrolyte can deliver a high reversible capacity of  $293 \text{ mA h g}^{-1}$  at  $-20^{\circ}\text{C}$ . Especially, when coupled with high mass-loading  $\text{LiFePO}_4$  (LFP,  $18.8 \text{ mg cm}^{-2}$ ) and Gr ( $8.3 \text{ mg cm}^{-2}$ ) electrodes, the single-layer pouch cell exhibits a high reversible capacity of  $84.85 \text{ mA h g}^{-1}$  under  $-40^{\circ}\text{C}$ , corresponding 66.28% capacity retention of the room-temperature capacity. The assembled 2.5 Ah LFP||Gr pouch cell achieves 96.85% capacity retention of its room-temperature capacity when charged at  $-20^{\circ}\text{C}$ .

## 2 | EXPERIMENTAL SECTION

### 2.1 | Preparation and characterization

LiODFB (99.9%), LiFSI (99.9%), fluoroethylene carbonate (FEC, 99.9%), EA (99.9%), N-methyl pyrrolidine (NMP; 99.5%) were purchased from Sigma-Aldrich. Polyvinylidene fluoride (PVDF) binder was purchased from Kynar. The commercial electrolyte of 1 M lithium hexafluorophosphate ( $\text{LiPF}_6$ ) in EC/dimethyl carbonate (DMC) (5:5 volume ratio) was directly bought from DoDoChem. The Gr powder was bought from Sinopharm Chemical Reagent Co., Ltd. EA and FEC were dried by molecular sieves ( $4 \text{ \AA}$ , Sigma-Aldrich) before formulating the electrolytes to remove the residual moisture in solvents. The LiFSI and LiODFB with ratio of 1:9, were dissolved and stirred in EA/FEC (95:5 volume ratio) for 12 h

(labeled as 1F9B), in which the total lithium salt concentration is set to 1 M. The electrolytes were prepared in the Ar-filled glovebox filled with water and oxygen less than 0.1 ppm. For coin cells, the Gr electrodes were prepared by coating a slurry composed of 80 wt% Gr powder, 10 wt% PVDF binder in NMP solution and 10 wt% conductive carbon (Super P) onto Cu foil. Then the electrodes were dried at 80°C for 12 h under vacuum. The mass loading of Gr is 1.5–2 mg cm<sup>-2</sup>. The LiFePO<sub>4</sub> (LFP) cathodes were also prepared by coating a slurry composed of 80 wt% LFP, 10 wt% PVDF binder in NMP solution, and 10 wt% conductive carbon (Super P) onto Al foil. The LFP electrodes were dried at 110°C for 12 h under vacuum. The mass loading of LFP is 3.5–4.5 mg cm<sup>-2</sup>. For pouch cells, the loading mass of LFP and Gr is ~18.8 and ~8.3 mg cm<sup>-2</sup> for a single side. The proportion of active materials in LFP and Gr is 94.3% and 93.3%, respectively.

The ionic conductivity ( $\sigma$ ) of electrolytes was measured by electrochemical impedance spectroscopy (EIS), two stainless-steel electrodes were symmetrically placed in the electrolytes. The values of  $\sigma$  were calculated based on the electrochemical impedance according to the following equation:

$$\sigma = \frac{L}{A * R},$$

where  $R$  is the measured resistance,  $A$  and  $L$  represent the area and the distance between the electrodes, respectively. The frequency range was controlled within 10<sup>6</sup> to 0.1 Hz with an AC amplitude of 10 mV. Cyclic voltammetry (CV) was tested in the Gr||Li cells from 2 to 0.01 V at the scan rate of 0.1 mV s<sup>-1</sup>. The CV and EIS were measured using Solartron Analytical 1260–1287 with AC impedance spectra capability. To investigate the freezing point of EA-based and conventional electrolytes, differential scanning calorimetry (DSC) was measured by using a NETZSCH DSC 204 F1 Phoenix. At Ar atmosphere, samples were cooled down to -80°C at a rate of 10°C min<sup>-1</sup>, then heated up from -80°C to 25°C at the rate of 2°C min<sup>-1</sup>. The onset temperature of the melting point was confirmed as the freezing point. Raman spectra of electrolytes were recorded on Renishaw in Via RM200. The excitation laser is 532 nm. X-ray photoelectron spectroscopy (XPS) was used to analyze the SEI components on Thermo Scientific (ESCALAB 250Xi). The results were calibrated by the C 1 s level (284.8 eV). The change of chemical composition of SEI was characterized by the time-of-flight secondary-ion mass spectroscopy (TOF-SIMS) on PHI nano TOF II. It was measured with Ar-ion gun with 3 kV energy and the sputter rate was about ~10.5 nm min<sup>-1</sup>. Transmission

electron microscope (TEM) was used to observe the thickness of SEI after cycled. TEM was performed with JEOL LEM-F200 and the accelerating voltage was 200 kV. It was noted that before the characterization of cycled samples, the electrode samples were retrieved from cells which had charged/discharged 5 cycles, then washed using EA solvent to remove the residual electrolyte. Finally, the electrode materials were dried under vacuum and ready for testing.

## 2.2 | Electrochemical measurements

All testing 2032 coin-type cells were assembled in Ar-filled glove box. The Gr electrode, Celgard 2500 (polypropylene) separator, and Li metal chip were sandwiched together in the Gr-Li half cell with 50  $\mu$ L electrolyte. The galvanostatic charge/discharge measurements were conducted in the voltage range of 0.01–2 V. The current density corresponding to 1 C is 372 mA g<sup>-1</sup>. The LFP||Li coin cells were assembled by lithium chip, Celgard 2500 and LFP electrode with 50  $\mu$ L electrolyte. The LFP||Li cells were tested in the voltage range of 2.5–4.2 V at a rate of 1 C (170 mA g<sup>-1</sup>). For the low temperature test, all coin cells were first charged/discharged at 0.5 C for 5 cycles, and then were transferred into a low-temperature chamber (CHINA-SCICOOING(BEIJING) SCIENCE & TECHNOLOGY), kept under required temperature for at least 2 h and then charged/discharged at 0.1 C. The coin-typed LFP||Gr full cells were assembled by Gr, Celgard 2500 and LFP electrode with 50  $\mu$ L electrolyte. The N/P ratio is set to 1.1 and the C-rate is calculated based on the mass of LFP cathode. The LFP||Gr pouch cells were assembled a semiautomated cell-manufacturing line in an Ar-filled glove box. The LFP cathode, Gr anode and separator are assembled on a Z-stacking machine. The 2.5 Ah pouch cell is composed of 16-layers Gr anode, 15-layers LFP cathode and 12 g electrolyte. For the charged/discharged capacity test under low temperatures, the cells were galvanostatically charged to 4 V at 0.1 C and potentiostatically charged until the current reached C/20, then discharged to 2 V at 0.1 C. Battery testers (Wuhan LAND Electronics) were used for electrochemical test. For the charge capacity test at -20°C, the 2.5 Ah pouch cell was galvanostatically charged to 3.65 V and then potentiostatically charged until the current reached C/20.

## 2.3 | Computational details

The Molecular Dynamics (MD) simulation of the lithium-ion electrolyte system was carried out using the Gromacs

program suite,<sup>26</sup> with the all-atom optimized potentials for liquid simulations (OPLS-AA) force field. The OPLS-2009IL force field parameters for  $\text{PF}_6^-$  were obtained from previous studies.<sup>27</sup> The force field parameters for other organic molecules, including EC, DMC, FEC, and EA were all generated using the AuToFF web server. The initial simulation boxes, with dimensions of  $60 \times 60 \times 60 \text{ \AA}^3$ , were created using the packmol program and contained the electrolyte components.<sup>28</sup> The structures were first energy-minimized and then annealed from 0 to 298.15 K over a 1 ns time period, with a time step of 1 ps, to reach an equilibrium state. The temperature was maintained at 298.15 K using the velocity-rescale thermostat with a relaxation constant of 1 ps.<sup>29</sup> The pressure was maintained at  $1.01325 \times 10^5 \text{ Pa}$  using Berendsen's barostat with an isothermal compressibility constant of  $4.5 \times 10^{-5}$ . Periodic boundary conditions were applied in all directions, and the electrostatic interactions and van der Waals forces were treated using the Particle-mesh Ewald method with a cut-off distance of  $10 \text{ \AA}$ . Following the energy-minimization and equilibration steps, a 20 ns MD simulation was performed, with the trajectory saved every 1 ps. The results, including radial distribution function (RDF), coordination number (CN) and dominant solvation clusters were analyzed using Gromacs tool-suites, the Visual MD program,<sup>30</sup> and additional scripts written by the researchers. The solvation structures of  $\text{Li}^+(\text{EC})_3(\text{DMC})_2$  and  $\text{Li}^+\text{DFOB}^-(\text{EA})_3$  are selected from two electrolyte systems respectively to compare the desolvation free energy. These two complex structures were optimized under the framework of density of functional theory (DFT) with m062x functional<sup>31</sup> and 6-31+G(d, p) basis set.<sup>32</sup> The vibrational frequency analysis is carried out for the optimized structure with the same calculation method to obtain the zero-point energy and free energy corrections. To obtain the electron energy with higher accuracy which has a major impact on the accuracy of Gibbs free energy, a single point calculation for the optimized structure with M06-2x functional and 6-311+G(d,p) basis set was performed.<sup>33</sup> Finally, the single point energy is added to the free energy correction calculated before to obtain the Gibbs free energy. The desolvation free energy of  $\text{Li}^+(\text{Ligand})_n$  was calculate from the formula:

$$G(\text{des}) = n \times G(\text{Ligand, sol}) + G(\text{Li}^+, \text{gas}) \\ - G(\text{Li}^+(\text{Ligand})_n, \text{sol}).$$

To calculate the reduction potentials of these electrolyte components, these solvent molecules, including FEC, EA, FSI, and DFOB and their anionic radicals formed after obtaining an electron were all optimized using M06-2x functional and 6-311+G(d,p) basis set.

Both explicit lithium ion and the implicit solvent model of SMD (Solvation Model Based on Density) were all applied to describe the solvation effect.<sup>34</sup> The vibrational frequency analysis was carried out for these optimized structure to the zero-point energy. The Gibbs free energy change and reduction potential of the reduction reaction of solvent molecule was calculated according to the formula below:

$$\Delta_{\text{red}} G = G(\text{initial}) - G(\text{reduction}),$$

$$\varphi_{\text{red}}(\text{vs. Li}^+/\text{Li}) = -\frac{\Delta_{\text{red}} G}{nF} - 1.45\text{V},$$

where  $G(\text{initial})$  and  $G(\text{reduction})$  are the Gibbs free energy of initial and reduction states of the molecule,  $F$  is the Faraday constant, 1.45 V is the standard potential of  $\text{Li}^+/\text{Li}$  electrode relative to vacuum level.

### 3 | RESULTS

For the design of low-temperature electrolytes, EA was selected as the solvent according to its ultralow melting point ( $-84^\circ\text{C}$ ) and much lower dielectric constant (6.4) than EC (90.1). Generally, the solvents with low dielectric constant have milder solvation effects on binding energy,<sup>35</sup> which is beneficial to the construction of weakly solvated electrolytes. LiODFB with weak dissociation ability was chosen as the main lithium salt to weaken the solvation effect because the weak dissociation facilitates anions to participate in the inner solvation structure.<sup>36,37</sup> And little LiFSI with strong dissociation ability was added to improve ionic conductivity.<sup>37</sup> The optimized dual-anion electrolyte is 0.1 M LiFSI + 0.9 M LiODFB in EA/FEC (95/5, vol%), donated as 1F9B, with a total concentration of electrolytes at 1 M. The single-salt electrolytes 10F (1 M LiFSI in EA/FEC [95/5, vol%]) and 10B (1 M LiODFB in EA/FEC [95/5, vol%]) were prepared to highlight the performance advantages of 1F9B (Supporting Information: Figure S1). For comparison, the commercial LP30 electrolyte (1 M  $\text{LiPF}_6$  in EC/DMC [5/5, vol%]) was also fabricated.

#### 3.1 | The physicochemical properties and solvation structures of electrolytes

The ionic conductivity ( $\sigma$ ) of the LP30 and 1F9B was measured and displayed in Figure 1A and Supporting Information: Table S1. It can be clearly seen that the ionic conductivity of 1F9B electrolyte is significantly higher than that of LP30, especially at temperatures



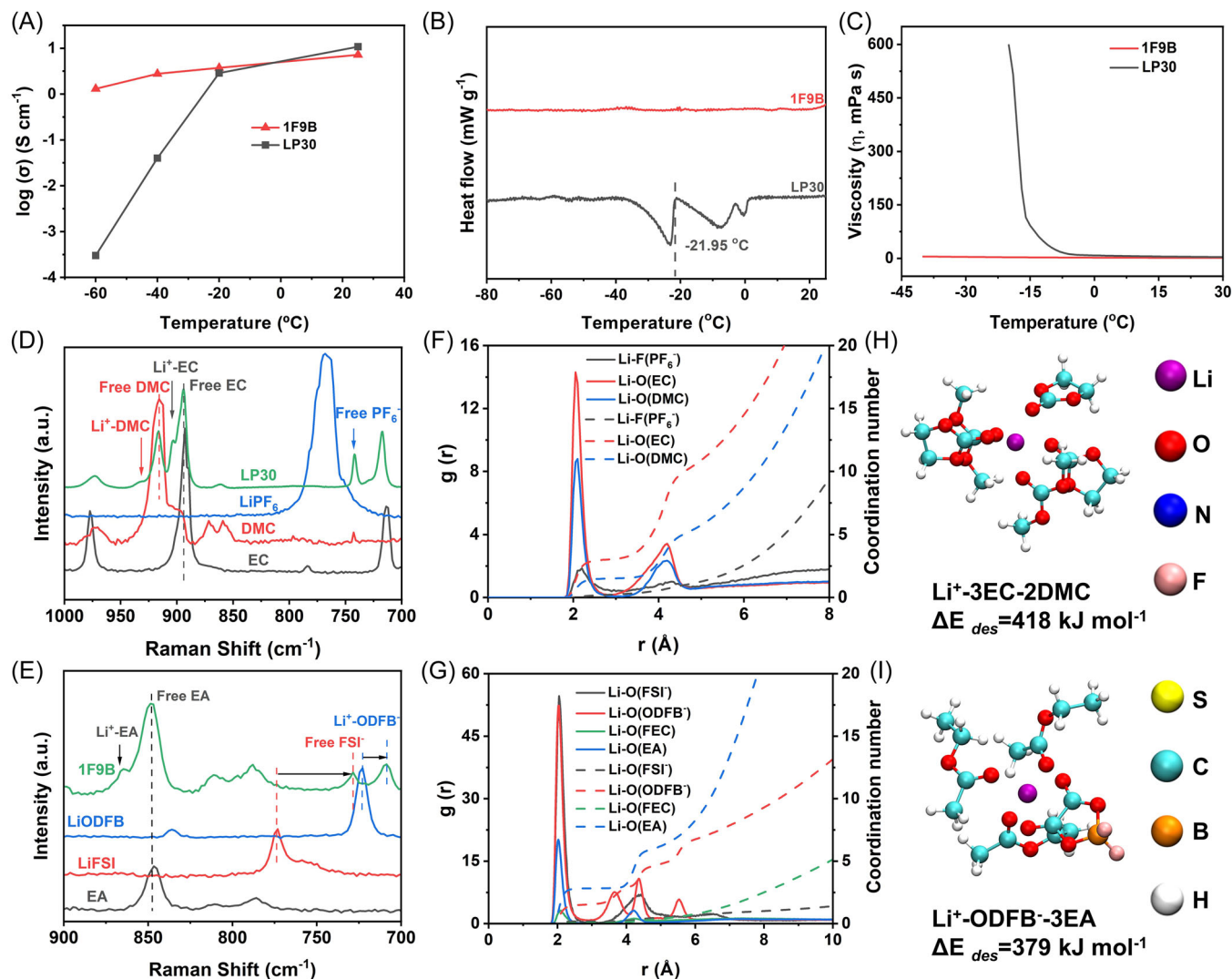


**FIGURE 1** The characterization of basic physicochemical properties and solvation structure for different electrolytes. (A) Ionic conductivity measured from -60°C to 25°C. (B) Differential scanning calorimetry heating curves from -80°C to 25°C. (C) Temperature-dependent viscosity investigation. Raman spectrum of (D) LP30 and (E) 1F9B with corresponding control groups. RDFs of (F) LP30 and (G) 1F9B. The primary solvation structures and desolvation energy of (H) LP30 and (I) 1F9B.

below -20°C. Specifically, the ionic conductivity of 1F9B is up to 1.30 mS cm<sup>-1</sup> even at -60°C, whereas that of LP30 rapidly drops below -20°C. Furthermore, DSC was performed to realize the phase transition in various electrolytes (Figure 1B). The results demonstrate that there is no phase transition for the EA-based electrolyte from 25°C to -80°C. On the contrary, the LP30 has a higher freezing point at -21.9°C. The viscosity of 1F9B and LP30 at various temperatures was also measured. At -40°C, the viscosity of 1F9B is 5.031 mPa s, while that of LP30 at -20°C is up to 598.5 mPa s (Figure 1C).

The regulated effects of dual anions on the solvation structures were analyzed by Raman spectroscopy and MD simulation. Figure 1D shows the Raman spectra of LP30, in which the peaks of 891 and 913 cm<sup>-1</sup> correspond to the free EC and DMC, respectively. After

adding LiPF<sub>6</sub>, these peaks shift to 901 and 933 cm<sup>-1</sup>, indicating the interaction between Li<sup>+</sup> and solvents.<sup>38</sup> A new peak at 740 cm<sup>-1</sup> belongs to the free PF<sub>6</sub><sup>-</sup>. In the Raman spectra of 1F9B (Figure 1E), the dissolution of LiFSI or LiODFB results in a blue shift in the C-C stretching vibration bond in EA from 848 cm<sup>-1</sup> to 854 cm<sup>-1</sup>, suggesting the solvation of EA with Li<sup>+</sup>. The peak at 774 cm<sup>-1</sup> for LiFSI after dissolution significantly red shift to 730 cm<sup>-1</sup>, corresponding to free FSI<sup>-</sup>.<sup>39</sup> While the peak of LiODFB at 722 cm<sup>-1</sup> shows a much smaller red shift, suggesting the strong interaction between Li<sup>+</sup> and ODFB<sup>-</sup>. These results are also well consistent with the Fourier transform infrared spectroscopy of electrolytes (Supporting Information: Figure S2). MD simulation is carried out to simulate the solvation structure of electrolytes. The RDFs of LP30 indicates that the Li<sup>+</sup>

coordination is controlled by EC and DMC and the CN of EC, DMC are 2.9, 1.6, respectively (Figure 1F). While in the RDFs of 1F9B (Figure 1G), the  $\text{Li}^+$  inner solvation sheath contains both  $\text{ODFB}^-$  and EA and the CN of  $\text{ODFB}^-$ , EA are 1.8, 3.2, respectively. In conclusion, the primary solvation sheath of LP30 is  $\text{Li}^+ \cdot 3\text{EC} \cdot 2\text{DMC}$ , which corresponds to a characteristic solvent-separated ion pair (SSIP) structure (Figure 1H, Supporting Information: Figure S3). While the major solvation structure in 1F9B is  $\text{Li}^+ \cdot \text{ODFB}^- \cdot 3\text{EA}$ , which is a representative CIP solvation structure (Figure 1I). Furthermore, the desolvation energy of two primary solvation structures are calculated by DFT. It can be found that the desolvation energy of 1F9B ( $379 \text{ kJ mol}^{-1}$ ) is much smaller than that of LP30 ( $418 \text{ kJ mol}^{-1}$ ), indicating the faster  $\text{Li}^+$  desolvation kinetics in 1F9B, which may facilitate  $\text{Li}^+$  transport on Gr/electrolyte interphase when charged at low temperatures.

### 3.2 | The electrochemical behaviors of Gr electrode

The Gr||Li half cells were assembled to evaluate the electrochemical behavior of Gr electrode in the designed electrolytes. Figure 2A shows discharge/charge curves of cells during the first cycle when cycled at room temperature. In 1F9B electrolyte,  $\text{FSI}^-$  and  $\text{ODFB}^-$  exhibit the reductive potential plateau at around 1.1 and 1.6 V, respectively. And the reduction in LP30 starts from  $\sim 0.7 \text{ V}$ , resulting from the decomposition of EC for forming film on the Gr surface. The rate capability of Gr||Li cells in 1F9B and LP30 was presented in Figure 2B. When the current density varied from 0.1 to 5 C, the cell using 1F9B shows an overwhelming advantage in capacity retention. Particularly, a much higher capacity of  $304 \text{ mA h g}^{-1}$  along with the highly reversible charge/discharge behavior are achieved in

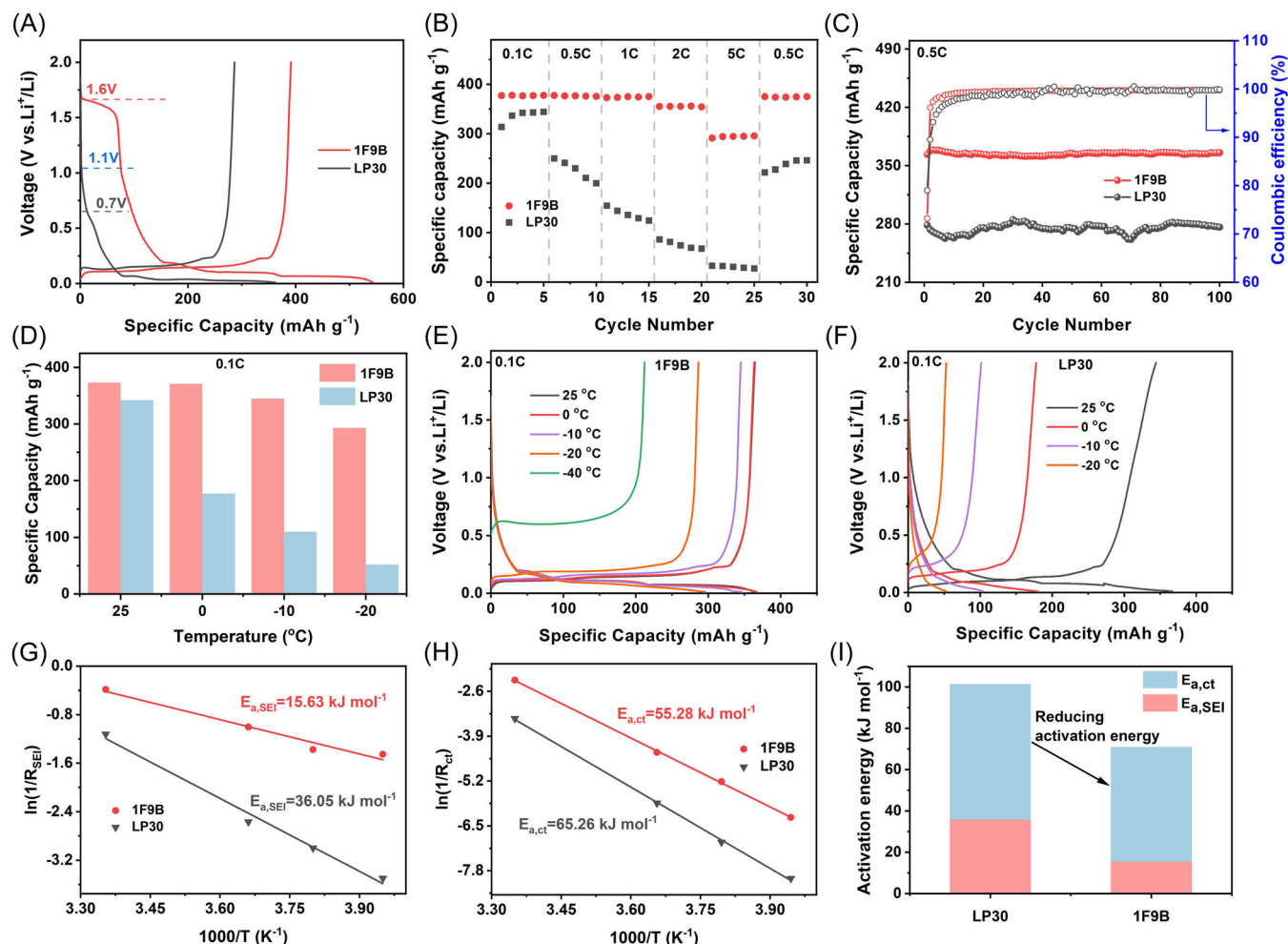


**FIGURE 2** Electrochemical performance and kinetics of interface on the graphite (Gr) electrode. (A) The charge/discharge curves of the first cycle. (B) Rate performance and (C) cycling stability at room temperature. (D) The specific capacity of Gr electrodes with LP30 and 1F9B at different temperatures. Charge/discharge curves of (E) 1F9B and (F) LP30 at different temperatures. Activation energies of (G)  $\text{Li}^+$  ions transport in the solid electrolyte interphase and (H) the charge transfer process. (I) The comparison of total activation energy.

1F9B at 5 C. In contrast, the cell using LP30 only shows a capacity of 25 mA h g<sup>-1</sup>. The long-term cycling stability of different electrolytes is shown in Figure 2C. The cell with 1F9B shows a higher specific capacity and almost no obvious capacity decay over 100 cycles. The superior rate and cycle performance of 1F9B may be ascribed to the fast desolvation process and superior Li<sup>+</sup> kinetics in SEI. Furthermore, the delivered capacities of Gr||Li cells with 1F9B and LP30 at low temperatures are compared in Figure 2D. The charge/discharge curves of Gr electrodes at different temperatures also indicate the lower polarization in 1F9B at low temperature is related to improved interfacial kinetics (Figure 2E,F). It can be found that the cells using 1F9B deliver a higher reversible capacity of 293 mA h g<sup>-1</sup> at -20°C, corresponding to 79.2% of its room-temperature capacity, while the cell using LP30 only exhibits a 15.11% capacity retention (52 mA h g<sup>-1</sup>). When discharging at -20°C and charging at -40°C, the cell with 1F9B can still retain a high capacity of 212 mA h g<sup>-1</sup>. Besides, the 1F9B electrolyte enables Gr||Li cell to exhibit approximately 100% charging capacity retention (Li<sup>+</sup> extraction from Gr) even at -60°C (Supporting Information: Figure S4). The average delithiation potentials of Gr electrode were monitored to investigate the polarization of cells at low temperatures. The cell presents the lower average delithiation potentials (-40°C: 0.3 V, -60°C: 0.8 V vs. Li<sup>+</sup>/Li) demonstrating the faster electrochemical reaction kinetics in 1F9B, while Gr||Li cell with LP30 fails to work at -60°C (Supporting Information: Figure S5). Due to that Li<sup>+</sup> interfacial behaviors on Gr electrode are considered to be the rate-determine steps to dominate the cell performance at low temperatures.<sup>40,41</sup> EIS measurements were carried out to further probe the Li<sup>+</sup> interfacial kinetics on Gr electrode (Supporting Information: Figure S6). By equivalent circuit fitting, the values of  $R_{SEI}$  and  $R_{ct}$  at selected temperatures are listed at Supporting Information: Tables S2 and S3. It can be found that both  $R_{SEI}$  and  $R_{ct}$  present a sharply increase when the cells operating at low temperatures. Moreover, the activation energy ( $E_a$ ) of Li<sup>+</sup> interfacial migration on Gr electrode was calculated based on the Butler–Volmer equation and Arrhenius equation, the relationship between  $R_{ct}/R_{SEI}$  and  $E_a$  is generalized as:

$$k = A \exp(-E_a/RT),$$

where  $k$  is the rate constant,  $A$  is the pre-exponential constant,  $T$  is the absolute temperature,  $R$  is the gas constant. As plotted in Figure 2G–I,  $E_a$  of both Li<sup>+</sup> transport in SEI and charge transfer process for Gr with 1F9B are 15.63 and 55.28 KJ mol<sup>-1</sup>, respectively, which are much lower than the cell with LP30 (36.05 and

65.26 KJ mol<sup>-1</sup>). The above results demonstrate the greatly enhanced kinetics on the Gr||Li cell with 1F9B electrolyte.

### 3.3 | The characteristic of SEI

The interphase chemistry, mainly regarding to the composition and structure of SEI, plays an important role in Li<sup>+</sup> diffusion behavior on Gr/electrolyte interphase and thus makes efforts to low-temperature performance.<sup>42</sup> The linear scan voltammetry (LSV) of 1 M LiFSI-EA electrolytes implies its poor electrochemical stability window (Supporting Information: Figure S7). And the cells with 1 M LiFSI-EA or 1 M LiODFB-EA can not work, which results from the severe decomposition of EA and the formation of unstable and thick SEI (Supporting Information: Figure S8). However, our designed electrolyte demonstrates the good compatibility of EA and Gr anode. CV profiles of Gr||Li cells reveal the SEI formation is dominated by EC reduction at ~0.7 V in LP30, ODFB<sup>-</sup> and FSI<sup>-</sup> reduction at ~1.6 and ~1.1 V in 1F9B, respectively (Figure 3A, Supporting Information: Figure S9). Moreover, the electrochemical window of 1F9B electrolyte was tested by LSV (Supporting Information: Figure S10). The reductive potential is at about 1.6 and 1.1 V, which is consistent with CV test. To give a relative reference about the redox order of each component in the 1F9B electrolytes, DFT calculations were performed to investigate the highest occupied molecular orbital and lowest unoccupied molecular orbital (LUMO) energy of different molecules in the electrolytes (Supporting Information: Figure S11). The LUMO energy of LiODFB (-1.43 eV), LiFSI (0.23 eV) are much lower than EA (0.49 eV), suggesting that they may be preferentially reduced than EA molecule. Furthermore, the reduction potentials of Li<sup>+</sup>-solvent, LiFSI and LiODFB were calculated (Supporting Information: Figure S12). The reduction potentials of LiFSI, LiODFB are 1.223 and 1.774 V, respectively, which is higher than that of Li<sup>+</sup>-EA (0.614 V). So the preferential decomposition of anions contributes to the construction of inorganic-rich SEI. Then the excellent characteristics of SEI formed by 1F9B have also been confirmed. The thickness of the SEI after 5 cycles was characterized by HRTEM (Figure 3B). The Gr anode used 1F9B presents the thin and uniform SEI layer (~2–4 nm), while the thickness of SEI in LP30 is ~10–12 nm, corresponding to three times thicker than that of 1F9B. The composition of SEI formed in the different electrolytes were characterized by XPS. The XPS spectra of pristine Gr electrode was presented in Supporting Information: Figure S13. The SEI on Gr electrode after 5 cycles was characterized by XPS. In the spectrum of C 1s (Figure 3C), the peaks at 284.8 and



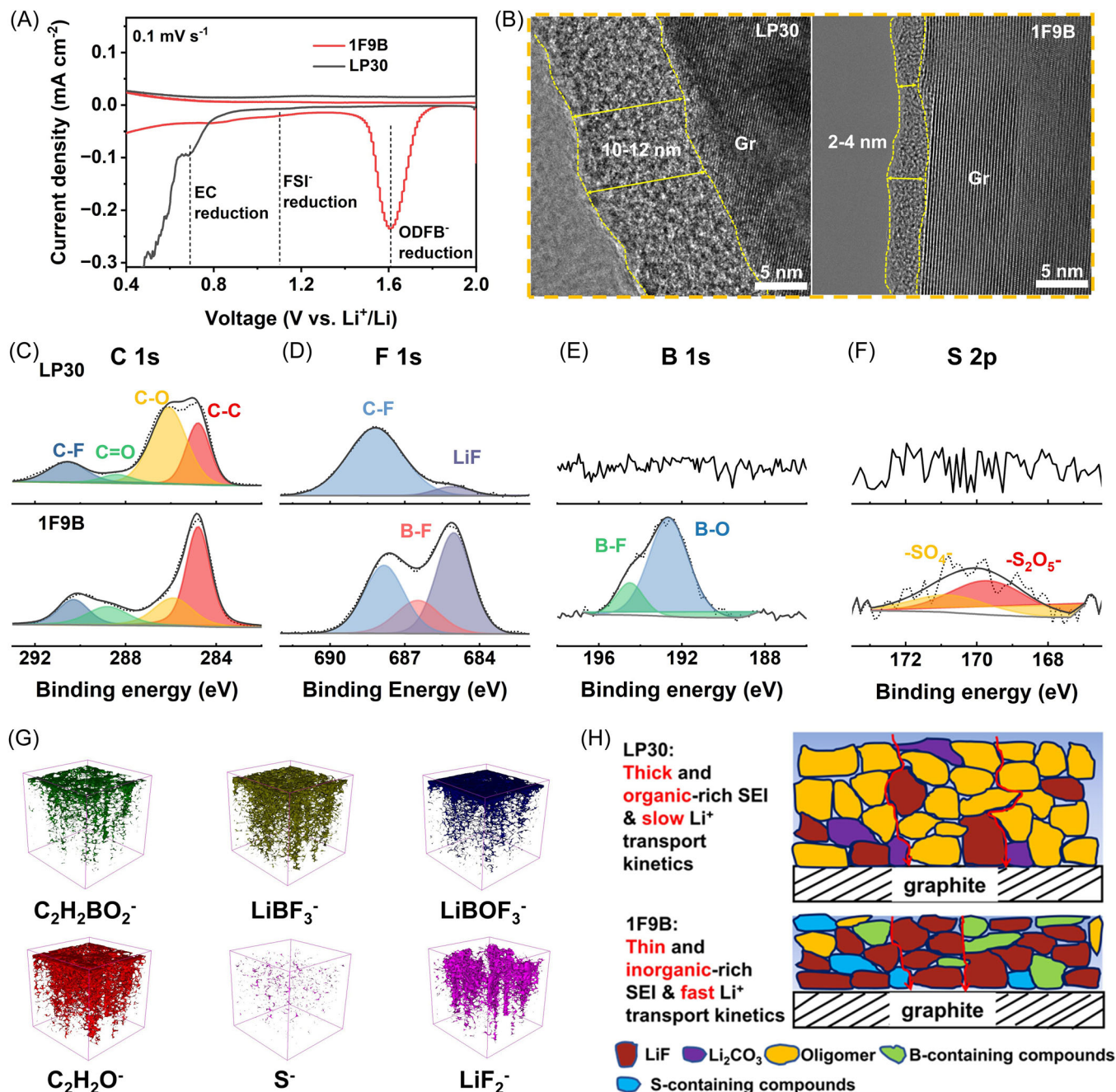


**FIGURE 3** The characteristic of solid electrolyte interphase on the graphite (Gr) anode. (A) Cyclic voltammetry scan of Gr||Li half cells with 1F9B and LP30. (B) The transmission electron microscope images of Gr electrodes cycled with LP30 and 1F9B. X-ray photoelectron spectroscopy spectra: (C) C 1 s; (D) F 1 s; (E) B 1 s; (F) S 2 p. (G) 3D views of different species from time-of-flight secondary-ion mass spectroscopy for 1F9B. (H) Schematic illustration of SEI features for LP30 and 1F9B.

290.6 eV correspond to C–C (from acetylene black and Gr) and C–F species (mainly from the PVDF binder), respectively. Generally, C–O (~285.9 eV) and C=O (~288.8 eV) are assigned to the carbon-containing organic (ROCO<sub>2</sub>Li, CH<sub>2</sub>OCO<sub>2</sub>Li) in SEI from the decomposition of solvents (such as carbonates and carboxylate).<sup>43</sup> The extraordinary low contents of C–O and C=O manifest that the decomposition of EA has been effectively

suppressed. Moreover, the F 1 s spectrum indicates much higher LiF in dual-anion regulated electrolyte derived from the reduction of LiFSI, LiODFB and FEC (Figure 3D).<sup>44–46</sup> As a typical SEI ingredient, LiF has high surface energy, a relatively lower lithium-ion diffusion energy barrier, and lower electronic conductivity, favoring rapid diffusion of Li<sup>+</sup> ions while suppressing interfacial side reactions.<sup>47–49</sup> Specifically, the B–F species and B–O



species ( $\text{Li}_x\text{BF}_y$ ,  $\text{Li}_x\text{BO}_y\text{F}_z$ ) in 1F9B come from the reduction of LiODFB, which was also detected in B 1s spectrum (Figure 3E). The B–F species have been confirmed to be the effective ingredients to enhance the stability of SEI and contribute to the improved cycle capability of batteries.<sup>50–52</sup> In the S 2p spectrum (Figure 3F), the appreciable S-containing components ( $-\text{S}_2\text{O}_5-$  [169.7 eV] and  $-\text{SO}_4-$  [170.8 eV]) originate from the decomposition of LiFSI in 1F9B, which can serve as the effective ingredients to decrease the interface resistance and facilitate the  $\text{Li}^+$  diffusion on Gr surface.<sup>53</sup> Moreover, the detailed morphology and structure of the SEI formed in the 1F9B electrolyte were further investigated by TOF-SIMS (Supporting Information: Figure S14). The sputter depth is calibrated on the basis of  $\text{SiO}_2$  sputtering rate. The intensity of  $\text{F}^-$  is the highest, indicating the formation of fluorinated SEI. At the surface,

the contents of  $\text{C}_2\text{H}_2\text{O}^-$ ,  $\text{BO}_2^-$ ,  $\text{C}_2\text{H}_2\text{BO}_2^-$ ,  $\text{LiBF}_3^-$ , and  $\text{LiB}_2\text{O}_4^-$  are observed and their intensities gradually drop down with the increase of sputtering depth, which proves the organic layer and B-containing compounds formed on the outer layer of SEI. The  $\text{LiF}_2^-$  content increases continuously and retains at a high level, suggesting the LiF is mainly in the inner layer of SEI. Also, the  $\text{S}^-$  signal shows a sharp increase with the sputtering, demonstrating the S-containing compounds are formed close to the inner layer. 3D-mapping images of SEI directly visualize the homogeneous coverage of inorganic-rich double-layer SEI (Figure 3G). Additionally, The uniform and thin SEI in 1F9B facilitates the accelerated  $\text{Li}^+$  transport and thus benefits the low-temperature properties. Figure 3H schematically illustrates the distribution features of SEI formed in 1F9B and LP30. For LP30, SEI is mainly composed of abundant organic products generated from

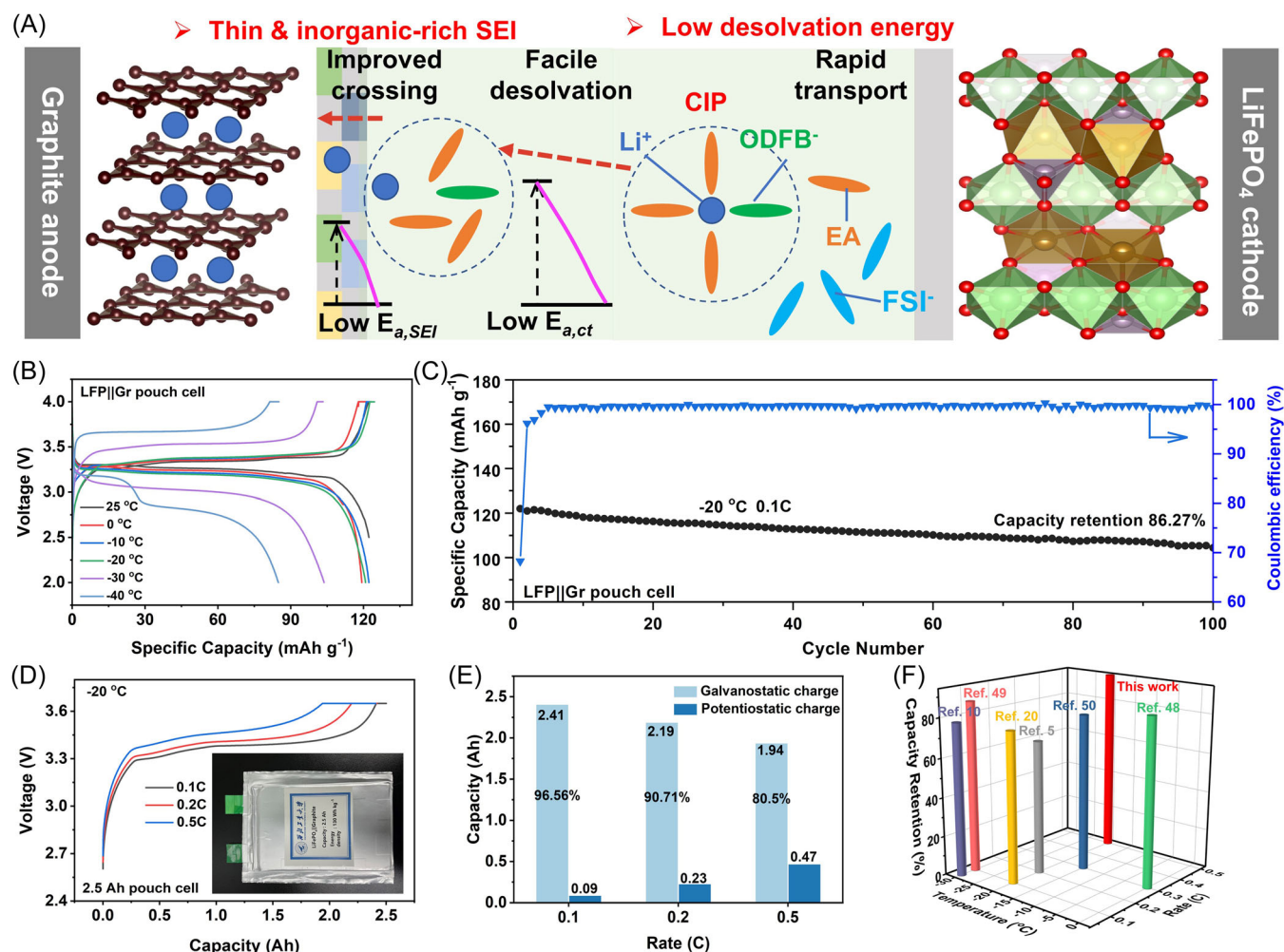


**FIGURE 4** Electrochemical performance of LFP||graphite (Gr) pouch cells with 1F9B. (A) Schematic illustration of LFP||Gr full cell. (B) Charge/discharge curves of single-layer pouch cell under different temperatures. (C) Cyclic stability of full cells at  $-20^{\circ}\text{C}$ . (D) The charging capacity of 2.5 Ah pouch cells at  $-20^{\circ}\text{C}$  with different rates. (E) The comparison of charging capacity by constant current and constant voltage at  $-20^{\circ}\text{C}$  with different rate. (F) The comparisons of capacity retention of rechargeable lithium-ion full cells at different rates and low temperatures with previously reported Gr-based lithium-ion batteries.

the decomposition of solvent EC and less inorganic matter from  $\text{LiPF}_6$ . But for 1F9B, SEI mainly consists of stacked inorganic compounds (B-containing compounds, S-containing compounds, and LiF) which significantly improves the interfacial kinetics. The unique interfacial chemistry is highly related to the solvation structure, which is deemed as the precursor of SEI. The primary solvation sheath of LP30 contains more solvents that form an organic-rich SEI on Gr anode. While the major solvation structure in 1F9B contains more anions and fewer solvents, resulting in anion-derived inorganic-rich SEI.

### 3.4 | The low-temperature performance of LFP||Gr full cell

Benefitting from low desolvation energy, high ionic conductivity, and inorganic-rich SEI (Figure 4A), LFP||Gr full cells with 1F9B also demonstrate excellent performance. The specific capacity of the full cell is calculated based on the mass of LFP and 1 C is equal to  $170 \text{ mA g}^{-1}$ . The coin-typed full cell shows stable cycle capability at room temperature (Supporting Information: Figure S15) and delivers a high reversible capacity when charged at  $-20^\circ\text{C}$  (Supporting Information: Figure S16). LFP||Gr pouch-typed full cells with 1F9B were assembled to further evaluate their electrochemical performance at subzero temperatures. As is well known, the rechargeability of Gr-based Li-ion full cells at low temperatures is challenging. However, the cell with 1F9B shows outstanding rechargeability under subzero temperature (Figure 4B). The single-layer pouch cell when charged at  $-20^\circ\text{C}$  with 0.1 C exhibits a reversible capacity of  $120 \text{ mAh g}^{-1}$  with a high capacity retention of 94.37%. At  $-30^\circ\text{C}$  and  $-40^\circ\text{C}$ , the cell can deliver capacities of 103.7 and  $84.85 \text{ mAh g}^{-1}$ , corresponding to 81.02% and 66.28% capacity retention of the room-temperature capacity. Moreover, the cell shows excellent cycle stability at  $-20^\circ\text{C}$  and maintains 86.27% of initial capacity after 100 cycles (Figure 4C). Surprisingly, the pouch cell can support a fan with LED (light emitting diode) working at  $-40^\circ\text{C}$  (Supporting Information: Video S1), indicating a considerable application prospect of the designed electrolyte at extremely subzero temperature. Furthermore, a 2.5 Ah pouch cell was assembled, as shown in Supporting Information: Figure S17. The cell can deliver a capacity of 1.37 Ah at 1 C when discharged at  $-40^\circ\text{C}$  (Supporting Information: Figure S18). When charged at  $-20^\circ\text{C}$ , the cell delivers a high reversible capacity of 2.5 Ah at 0.1 C, which retains 96.85% of its room-temperature capacity. More impressively, the cell can still keep a capacity of 2.41 Ah at a high current density of 0.5 C, corresponding to 93.86% of its room temperature capacity (Figure 4D). Additionally, it is

worth noting that the capacities of cells contributed by galvanostatically charging at 0.1 C and 0.5 C are up to 96.56% and 80.5%, respectively (Figure 4E). The outstanding charging performance of Ah-level pouch cell at low temperature further realistically demonstrates the superiority of our designed electrolyte. When compared to other reported low-temperature electrolytes for Gr-based lithium-ion full cells,<sup>5,12,24,54–56</sup> the cell with our designed electrolyte exhibits the highest capacity retention when charged at  $-20^\circ\text{C}$  and 0.5 C (Figure 4F), indicating the bright prospects of linear carboxylate-based electrolyte for low-temperature application in Gr-based LIBs.

## 4 | CONCLUSION

In summary, we regulated the solvation structure of EA-based electrolyte based on the conventional concentration of 1 M and improved the interfacial stability of EA with Gr anode. By virtue of the strong interaction between  $\text{Li}^+$  and  $\text{ODFB}^-$ , the designed electrolyte displays a typical CIP solvation structure and realizes reduced  $\text{Li}^+$  desolvation energy. Moreover, the preferential reduction of  $\text{ODFB}^-$  and  $\text{FSI}^-$  produces the inorganic-dominated SEI and thus facilitates  $\text{Li}^+$  migration. Consequently, the electrolyte enables Gr anode to deliver a considerable reversible capacity of  $293 \text{ mAh g}^{-1}$  and the 2.5 Ah LFP||Gr pouch cell to remain 96.85% of its room-temperature capacity at  $-20^\circ\text{C}$ . With high-loading electrodes (LFP cathode:  $18.8 \text{ mg cm}^{-2}$ ; Gr anode:  $8.3 \text{ mg cm}^{-2}$ ), the single-layer LFP||Gr pouch cell can still retain a high reversible capacity retention of 66.28% at  $-40^\circ\text{C}$ . This work offers effective guidelines for the design of high-performance linear carboxylate-based electrolytes for low-temperature Gr-based LIBs.

## ACKNOWLEDGMENTS

This work was supported by the National Key Research and Development Program of China (2023YFE0203000), the Natural Science Basic Research Plan in Shaanxi Province of China (2022JQ-086), Natural Science Foundation of Chongqing, China (CSTB2022NSCQ-MSX0596), the Hong Kong Scholars Program (XJ2021040), the Hong Kong Polytechnic University (G-YZ4S), the Fundamental Research Funds for the Central Universities (3102019JC005).

## CONFLICT OF INTEREST STATEMENT

The authors declare no conflict of interest.

## DATA AVAILABILITY STATEMENT

The data that support the findings of this study are available from the corresponding author upon reasonable request.

## ORCID

Ting Jin  <https://orcid.org/0000-0001-6521-5131>

## REFERENCES

- Xu K. Li-ion battery electrolytes. *Nat Energy*. 2021;6(7):763.
- Schmuck R, Wagner R, Höpkel G, Placke T, Winter M. Performance and cost of materials for lithium-based rechargeable automotive batteries. *Nat Energy*. 2018;3:267-278.
- Xue W, Qin T, Li Q, Zan M, Yu X, Li H. Exploiting the synergistic effects of multiple components with a uniform design method for developing low-temperature electrolytes. *Energy Storage Mater*. 2022;50:598-605.
- Fly A, Kirkpatrick I, Chen R. Low temperature performance evaluation of electrochemical energy storage technologies. *Appl Therm Eng*. 2021;189:116750.
- Nan B, Chen L, Rodrigo ND, et al. Enhancing Li<sup>+</sup> transport in NMC811||graphite lithium-ion batteries at low temperatures by using low-polarity-solvent electrolytes. *Angew Chem Int Ed*. 2022;61(35):202205967.
- Chen J, Zhang Y, Lu H, et al. Electrolyte solvation chemistry to construct an anion-tuned interphase for stable high-temperature lithium metal batteries. *eScience*. 2023;3(4):100135.
- Meng Y-F, Liang H-J, Zhao C-D, et al. Concurrent recycling chemistry for cathode/anode in spent graphite/LiFePO<sub>4</sub> batteries: designing a unique cation/anion-co-workable dual-ion battery. *J Energy Chem*. 2022;64:166-171.
- Luo D, Li M, Zheng Y, et al. Electrolyte design for lithium metal anode-based batteries toward extreme temperature application. *Adv Sci*. 2021;8(18):2101051.
- Chen L, Wu H, Ai X, Cao Y, Chen Z. Toward wide-temperature electrolyte for lithium-ion batteries. *Battery Energy*. 2022;1(2):20210006.
- Liang H-J, Gu Z-Y, Zhao X-X, et al. Advanced flame-retardant electrolyte for highly stabilized K-ion storage in graphite anode. *Sci Bull*. 2022;67(15):1581-1588.
- Fan X, Ji X, Chen L, et al. All-temperature batteries enabled by fluorinated electrolytes with non-polar solvents. *Nat Energy*. 2019;4(10):882-890.
- Yang Y, Fang Z, Yin Y, et al. Synergy of weakly-solvated electrolyte and optimized interphase enables graphite anode charge at low temperature. *Angew Chem Int Ed*. 2022;61(36):e202208345.
- Li WH, Li YM, Liu XF, et al. All-climate and ultrastable dual-ion batteries with long life achieved via synergistic enhancement of cathode and anode interfaces. *Adv Funct Mater*. 2022;32(21):2201038.
- Hubble D, Brown DE, Zhao Y, et al. Liquid electrolyte development for low-temperature lithium-ion batteries. *Energy Environ Sci*. 2022;15(2):550-578.
- Yi X, Feng Y, Rao AM, Zhou J, Wang C, Lu B. Quasi-solid aqueous electrolytes for low-cost sustainable alkali-metal batteries. *Adv Mater*. 2023;35(29):2302280.
- Yao YX, Chen X, Yan C, et al. Regulating interfacial chemistry in lithium-ion batteries by a weakly solvating electrolyte. *Angew Chem Int Ed*. 2021;60(8):4090-4097.
- Collins GA, Geaney H, Ryan KM. Alternative anodes for low temperature lithium-ion batteries. *J Mater Chem A*. 2021;9(25):14172-14213.
- Jiang LL, Yan C, Yao YX, Cai W, Huang JQ, Zhang Q. Inhibiting solvent co-intercalation in a graphite anode by a localized high-concentration electrolyte in fast-charging batteries. *Angew Chem Int Ed*. 2021;60(7):3402-3406.
- Flamme B, Rodriguez Garcia G, Weil M, et al. Guidelines to design organic electrolytes for lithium-ion batteries: environmental impact, physicochemical and electrochemical properties. *Green Chem*. 2017;19(8):1828-1849.
- Sazhin SV, Khimchenko MY, Trittenchenko YN, Lim HS. Performance of Li-ion cells with new electrolytes conceived for low-temperature applications. *J Power Sources*. 2000;87(1):112-117.
- Dong X, Guo Z, Guo Z, Wang Y, Xia Y. Organic batteries operated at -70°C. *Joule*. 2018;2(5):902-913.
- Lin S, Hua H, Lai P, Zhao J. A multifunctional dual-salt localized high-concentration electrolyte for fast dynamic high-voltage lithium battery in wide temperature range. *Adv Energy Mater*. 2021;11(36):2101775.
- Li Z, Yao N, Yu L, et al. Inhibiting gas generation to achieve ultralong-lifespan lithium-ion batteries at low temperatures. *Matter*. 2023;6(7):2274-2292.
- Yoo DJ, Liu Q, Cohen O, Kim M, Persson KA, Zhang Z. Rational design of fluorinated electrolytes for low temperature lithium-ion batteries. *Adv Energy Mater*. 2023;13(20):2204182.
- Yang Y, Li P, Wang N, et al. Fluorinated carboxylate ester-based electrolyte for lithium ion batteries operated at low temperature. *Chem Commun*. 2020;56(67):9640-9643.
- Abraham MJ, Murtola T, Schulz R, et al. Gromacs: high performance molecular simulations through multi-level parallelism from laptops to supercomputers. *SoftwareX*. 2015;1-2:19-25.
- Sambasivarao SV, Acevedo O. Development of OPLS-AA force field parameters for 68 unique ionic liquids. *J Chem Theory Comput*. 2009;5(4):1038-1050.
- Martínez L, Andrade R, Birgin EG, Martínez JM. Packmol: a package for building initial configurations for molecular dynamics simulations. *J Comput Chem*. 2009;30(13):2157-2164.
- Bussi G, Donadio D, Parrinello M. Canonical sampling through velocity rescaling. *J Chem Phys*. 2007;126(1):014101.
- Humphrey W, Dalke A, Schulten K. Vmd: visual molecular dynamics. *J Mol Graphics*. 1996;14(1):33-38.
- Zhao Y, Truhlar DG. The M06 suite of density functionals for main group thermochemistry, thermochemical kinetics, non-covalent interactions, excited states, and transition elements: two new functionals and systematic testing of four M06-class functionals and 12 other functionals. *Theor Chem Acc*. 2007;120(1-3):215-241.
- Clark T, Chandrasekhar J, Spitznagel GW, Schleyer PVR. Efficient diffuse function-augmented basis sets for anion calculations. III. The 3-21+G basis set for first-row elements, Li-F. *J Comput Chem*. 1983;4(3):294-301.
- Neese F, Wennmohs F, Becker U, Riplinger C. The orca quantum chemistry program package. *J Chem Phys*. 2020;152(22):224108.
- Marenich AV, Cramer CJ, Truhlar DG. Universal solvation model based on solute electron density and on a continuum model of the solvent defined by the bulk dielectric constant and atomic surface tensions. *J Phys Chem B*. 2009;113:6378-6396.



35. Yao N, Sun SY, Chen X, et al. The anionic chemistry in regulating the reductive stability of electrolytes for lithium metal batteries. *Angew Chem Int Ed*. 2022;61(52):e202210859.
36. Zhao Y, Hu Z, Zhao Z, et al. Strong solvent and dual lithium salts enable fast-charging lithium-ion batteries operating from  $-78$  to  $60^{\circ}\text{C}$ . *J Am Chem Soc*. 2023;145(40):22184-22193.
37. Mao M, Ji X, Wang Q, et al. Anion-enrichment interface enables high-voltage anode-free lithium metal batteries. *Nat Commun*. 2023;14(1):1082.
38. Wang X, Yang L, Ahmad N, Ran L, Shao R, Yang W. Colloid electrolyte with changed  $\text{Li}^{+}$  solvation structure for high-power, low-temperature lithium-ion batteries. *Adv Mater*. 2023;35:2209140.
39. Zhou T, Zhao Y, El Kazzi M, Choi JW, Coskun A. Integrated ring-chain design of a new fluorinated ether solvent for high-voltage lithium-metal batteries. *Angew Chem Int Ed*. 2022;61:202115884.
40. Holoubek J, Liu H, Wu Z, et al. Tailoring electrolyte solvation for Li metal batteries cycled at ultra-low temperature. *Nat Energy*. 2021;6:303-313.
41. Li Q, Lu D, Zheng J, et al.  $\text{Li}^{+}$ -desolvation dictating lithium-ion battery's low-temperature performances. *ACS Appl Mater Interfaces*. 2017;9(49):42761-42768.
42. Li X, Zhao R, Fu Y, Manthiram A. Nitrate additives for lithium batteries: mechanisms, applications, and prospects. *eScience*. 2021;1(2):108-123.
43. Zhao X, Yi R, Zheng L, et al. Practical prelithiation of 4.5 V  $\text{LiCoO}_2/\text{graphite}$  batteries by a passivated lithium-carbon composite. *Small*. 2022;18(9):2106394.
44. Zhang XQ, Chen X, Cheng XB, et al. Highly stable lithium metal batteries enabled by regulating the solvation of lithium ions in nonaqueous electrolytes. *Angew Chem Int Ed*. 2018;57(19):5301-5305.
45. Thenuwara AC, Shetty PP, Kondekar N, et al. Efficient low-temperature cycling of lithium metal anodes by tailoring the solid-electrolyte interphase. *ACS Energy Lett*. 2020;5(7):2411-2420.
46. Zhang XQ, Cheng XB, Chen X, Yan C, Zhang Q. Fluoroethylene carbonate additives to render uniform Li deposits in lithium metal batteries. *Adv Funct Mater*. 2017;27(10):1605989.
47. Zhang K, Wu F, Wang X, et al.  $8.5\text{ }\mu\text{m}$ -thick flexible-rigid hybrid solid-electrolyte/lithium integration for air-stable and interface-compatible all-solid-state lithium metal batteries. *Adv Energy Mater*. 2022;12(24):2200368.
48. Ding JF, Xu R, Yan C, Li BQ, Yuan H, Huang JQ. A review on the failure and regulation of solid electrolyte interphase in lithium batteries. *J Energy Chem*. 2021;59:306-319.
49. Tu S, Zhang B, Zhang Y, et al. Fast-charging capability of graphite-based lithium-ion batteries enabled by  $\text{Li}_3\text{P}$ -based crystalline solid-electrolyte interphase. *Nat Energy*. 2023;8:1365-1374.
50. Chen R, Zhu L, Wu F, Li L, Zhang R, Chen S. Investigation of a novel ternary electrolyte based on dimethyl sulfite and lithium difluoromono(oxalato)borate for lithium ion batteries. *J Power Sources*. 2014;245:730-738.
51. Liao B, Li H, Xu M, et al. Designing low impedance interface films simultaneously on anode and cathode for high energy batteries. *Adv Energy Mater*. 2018;8(22):1800802.
52. Song G, Yi Z, Su F, Xie L, Chen C. New insights into the mechanism of LiDFBOP for improving the low-temperature performance via the rational design of an interphase on a graphite anode. *ACS Appl Mater Interfaces*. 2021;13(33):40042-40052.
53. Jurng S, Park S, Yoon T, et al. Low-temperature performance improvement of graphite electrode by allyl sulfide additive and its film-forming mechanism. *J Electrochem Soc*. 2016;163(8):A1798-A1804.
54. Qian Y, Chu Y, Zheng Z, et al. A new cyclic carbonate enables high power/low temperature lithium-ion batteries. *Energy Storage Mater*. 2022;45:14-23.
55. Xu J, Zhang J, Pollard TP, et al. Electrolyte design for Li-ion batteries under extreme operating conditions. *Nature*. 2023;614:694-700.
56. Yao YX, Yao N, Zhou XR, et al. Ethylene carbonate-free electrolytes for rechargeable Li-ion pouch cells at subfreezing temperatures. *Adv Mater* 2022;34(45):2206448.

## SUPPORTING INFORMATION

Additional supporting information can be found online in the Supporting Information section at the end of this article.

**How to cite this article:** Che L, Hu Z, Zhang T, et al. Regulating the interfacial chemistry of graphite in ethyl acetate-based electrolyte for low-temperature Li-ion batteries. *Battery Energy*. 2024;3:20230064. doi:10.1002/bte2.20230064